
Origins and Scaling of Hot-Electron Preheat in Ignition-Scale Direct-Drive Inertial Confinement Fusion Experiments

Direct-drive inertial confinement fusion (ICF)^{1,2} is one of two laser-based techniques being pursued for achieving controlled nuclear fusion at the 1.8-MJ National Ignition Facility (NIF).³ In direct-drive hot-spot ignition designs, laser ablation of a spherical shell drives the implosion and compression of a cryogenic deuterium–tritium (DT) fuel layer, into which a fusion burn wave propagates after first being initiated in a central, low-density hot spot.⁴ To achieve ignition, the fuel must be compressed to an areal density greater than 0.3 g/cm², which can be achieved by keeping the pressure close to the Fermi-degenerate pressure. Preheat of the DT fuel by suprathermal electrons generated by laser–plasma instabilities (LPI’s) increases this pressure, degrades compression, and inhibits ignition. Consequently, control of LPI suprathermal (or “hot”)–electron production is critical for a successful implosion.

Stimulated Raman scattering (SRS)^{5–8} and two-plasmon decay (TPD)⁹ are two instabilities that are capable of generating hot electrons since they both excite electrostatic waves in the plasma that provide accelerating fields. SRS entails the decay of a laser light wave into an electron plasma wave and a scattered-light wave at densities at or below one quarter of the critical density of the laser, while TPD is the decay of a laser light wave into two electrostatic plasma waves (plasmons) near the quarter-critical density. Previous studies of SRS and TPD have examined single-beam thresholds,^{9,10} quantified suprathermal electron production,^{6,11,12} explored collective multibeam processes,^{13–18} and investigated the spatial properties of TPD¹⁹ and the angular distribution of the resulting hot electrons²⁰—an important consideration when computing preheat. SRS imposes serious constraints on ignition designs in the indirect-drive approach to ICF because of the high single-beam intensities and large volumes of quasi-homogeneous plasma that are required when using gas-filled hohlraums.²¹ To date, direct-drive experiments have shown minimal SRS resulting from lower single-beam intensities and density scale lengths shorter than ignition scale.

The low level or absence of observable SRS reflectivity in subscale (density scale length $L_n \sim 150 \mu\text{m}$ and electron temperature $T_e \sim 2 \text{ keV}$) direct-drive implosions on the OMEGA

laser [maximum laser energy (power) of 30 kJ (30 TW)] (Ref. 22) has focused work instead on the physics, scaling, and mitigation of TPD, which is observed close to threshold.¹⁵ Direct-drive implosions on OMEGA are known to excite collective multibeam TPD, which, at the highest-available irradiation intensities, converts as much as 1% of the incident laser energy to hot electrons. This level of hot electrons is close to what can be tolerated in direct-drive–ignition designs, and the scaling of hot-electron production to ignition scale has not yet been assessed. Ignition-scale direct-drive implosions²³ will have much longer density scale lengths ($L_n \sim 600 \mu\text{m}$) and hotter coronal electron temperatures ($T_e \lesssim 5 \text{ keV}$), placing the interaction conditions in a previously unexplored regime. Until the experiments described herein, carried out on a MJ-scale facility, it was not possible to simultaneously achieve the density scale length, laser intensity, electron temperature, and transverse plasma dimensions that are characteristic of ignition-scale direct-drive implosions.

This article presents the first exploration of the LPI origins, scaling, and possible mitigation of hot electrons under direct-drive ignition-relevant conditions. These new observations indicate the dominance of SRS over TPD, a result not previously anticipated, with significant implications for direct-drive–ignition designs.

Planar targets were irradiated from one side with 351-nm laser light using a subset of the NIF’s 192 beams, with 1-D smoothing by spectral dispersion²⁴ at 90 GHz. These beams are arranged into cones that share a common angle with respect to the polar axis. There are four such cones in each hemisphere: the “inner” cones have angles of 23.5° and 30° (32 beams in each hemisphere), while the “outer” cones have angles of 44.5° and 50° (64 beams in each hemisphere). All targets described here were irradiated using beams in the southern hemisphere. The targets were thick CH (or Si) disks with a 4.4-mm diameter and a 1.2-mm (or 0.75-mm) thickness, oriented toward a polar angle between 0° and 30°. Planar targets were chosen because they are the only way, currently, to achieve direct-drive ignition-relevant plasma conditions, while using a reduced laser energy (~200 kJ)

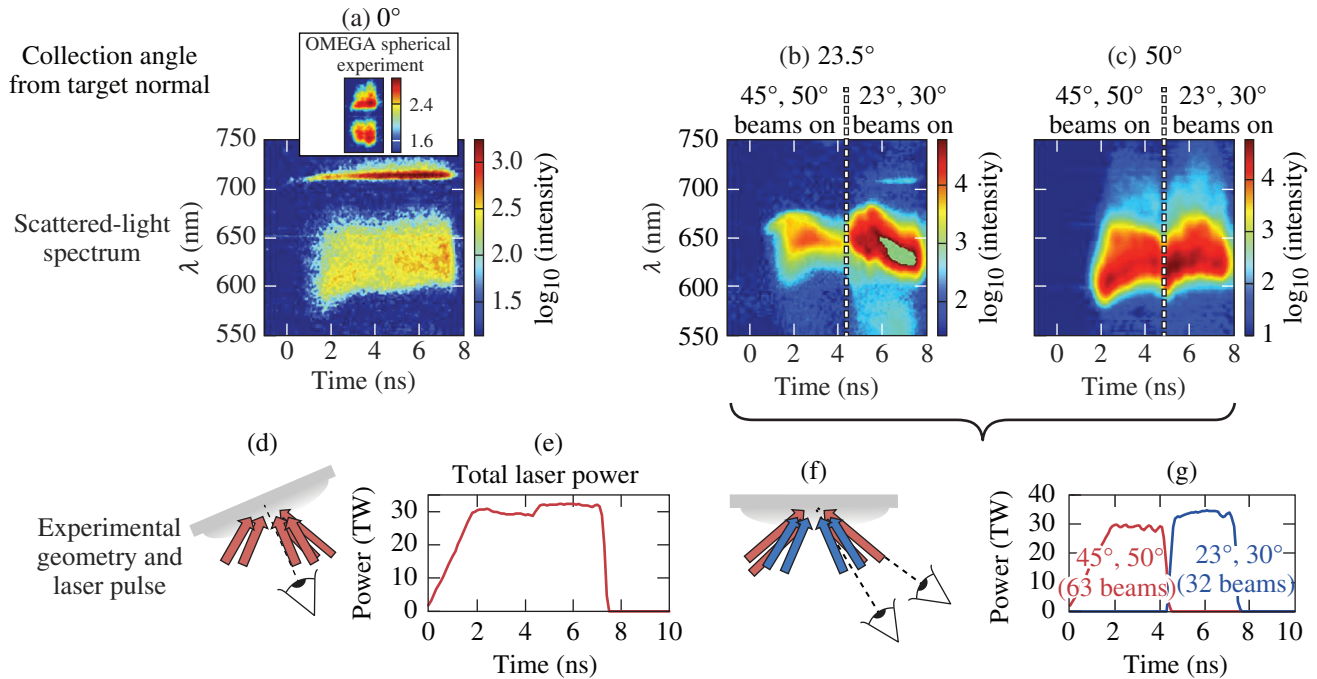
on the NIF. The use of planar targets also reduces the level of cross-beam energy transfer²⁵ relative to spherical targets.

Time-resolved SRS diagnostics, with or without spectral resolution (400 to 750 nm), were located at polar angles of 23.5°, 30°, and 50° (Ref. 26), as shown in Fig. 151.22. The targets were irradiated with laser pulses of ≤ 8 -ns duration at vacuum overlapped intensities of $\leq 3 \times 10^{15}$ W/cm². The plasma evolution was simulated using the 2-D radiation–hydrodynamics code *DRACO*²⁷ for comparison with experimental observations. The *DRACO* predictions for the density scale lengths and electron temperatures, in the vicinity of the quarter-critical density $n_e = n_c/4$ [where n_e is the electron density and n_c is the critical density for the laser wavelength λ_0 (in μm), with $n_c \approx 1.1 \times 10^{21} \lambda_0^{-2} \text{cm}^{-3}$] were $L_n \sim 500$ to $700 \mu\text{m}$ and $T_e \sim 3$ to 5 keV, respectively. *DRACO* simulations calculate that the laser intensity is attenuated by $\sim 50\%$ on reaching the quarter-critical surface as a result of collisional absorption.

A time-resolved scattered-light spectrum obtained from NIF shot N160420-003 is shown in Fig. 151.22(a). It displays a narrow, intense feature at a wavelength slightly above

702 nm ($2\lambda_0$). A local (i.e., near $n_c/4$) electron temperature measurement can be obtained from this feature from the relation $T_{e,\text{keV}} = \Delta\lambda_{\text{nm}}/3.09$ (Ref. 28), where $\Delta\lambda$ is the shift of the spectral peak from $2\lambda_0$ after corrections for Doppler and Dewandre shifts²⁹ have been applied.³⁰ The electron temperature inferred from this technique is $T_e = 4.5 \pm 0.2$ keV. The *DRACO* calculations predict a consistent temperature (4.5 keV), giving confidence in the numerical modeling of the corona and indicating that ignition-relevant temperatures have been achieved. As a result of refraction effects, this spectral feature is emitted only perpendicularly to the density gradient (i.e., along the target normal),¹⁹ and its observation required that the target be tilted to face the diagnostic [Fig. 151.22(d)]. For this reason, it is not seen in Figs. 151.22(b) or 151.22(c).

Importantly, this feature demonstrates significant differences relative to the near- $2\lambda_0$ spectrum obtained at smaller scales on OMEGA. A typical half-harmonic spectrum from a spherical implosion experiment (shot 80802) on OMEGA is shown in the inset of Fig. 151.22(a), sharing the same wavelength scale as the NIF spectrum. The characteristic half-harmonic features that are red- and blue-shifted with respect to $2\lambda_0$ seen

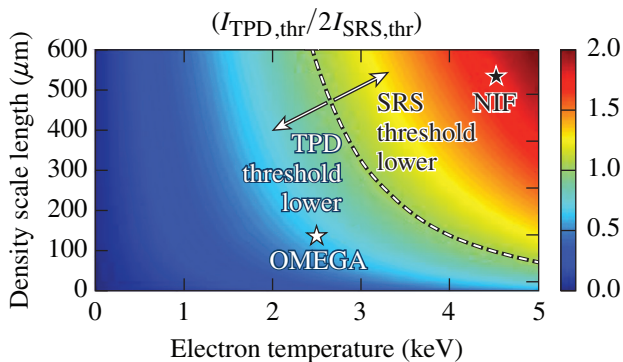


E26371JR

Figure 151.22 Time-resolved scattered-light spectra at collection angles of (a) 0°, (b) 23.5°, and (c) 50° relative to the target normal. These images were obtained in two CH target experiments. The image in (a) corresponds to an experiment (d) with the target oriented toward a streaked spectrometer and (e) irradiated by a ramp-flat pulse at a peak quarter-critical laser intensity of 1.3×10^{15} W/cm². The images in (b) and (c) correspond to an experiment (f) with the target oriented toward the south pole of NIF and was (g) irradiated first by beams at incidence angles of 45° and 50°, followed by beams at 23° and 30°. The streaked spectrum from a spherical-geometry experiment on OMEGA [inset in (a)] is contrasted to the image in (a).

in the OMEGA experiment are a definitive diagnostic of the presence of TPD.³¹ The doublet arises by processes such as inverse resonance absorption, inverse parametric decay, and self-Thomson scattering that convert the up- and down-shifted TPD daughter plasma waves into transverse (light) waves.²⁸ The lack of a blue-shifted half-harmonic and the narrowness of the red-shifted feature seen in the NIF experiment is a strong indication that different physical processes are occurring at the quarter-critical surface. The sharp feature observed in the NIF experiment is a well-known signature of the absolute Raman instability that can occur at densities close to quarter critical.²⁸ The OMEGA spectrum implies the absence of SRS around $n_c/4$ and the presence of TPD, while the NIF spectrum implies the presence of SRS at and below $n_c/4$. Although the presence of some TPD activity in the NIF experiment cannot be entirely ruled out on the basis of Fig. 151.22(a) since the conversion efficiencies of TPD waves to half-harmonic emission relative to absolute SRS are difficult to quantify, it seems most plausible that SRS, rather than TPD, is the dominant quarter-critical LPI mechanism in ignition-scale direct-drive experiments.

Simple considerations based on the absolute threshold intensities for SRS ($I_{14}^{\text{SRS,thr}} = 2377/L_{n,\mu\text{m}}^{4/3}$) and TPD ($I_{14}^{\text{TPD,thr}} = 233 T_{e,\text{keV}}/L_{n,\mu\text{m}}$), for normally incident single plane-wave beams,^{9,10} further support this identification. In these expressions, I_{14}^{thr} is the threshold intensity in units of 10^{14} W/cm². As an illustrative case, Fig. 151.23 shows the ratio of the absolute TPD threshold to twice that for absolute SRS as a function of electron temperature and density scale length. This



E26298JR

Figure 151.23

Ratio of absolute single-beam intensity threshold for two-plasmon decay (TPD)¹⁰ to twice the absolute, single-beam threshold for SRS⁹ (to acknowledge a potential difference in multibeam effects) as a function of electron temperature and density scale length. Conditions corresponding to the NIF (OMEGA) spectra in Fig. 151.22(a) are represented by the black (white) star. To the left (right) of the dashed line, the TPD (SRS) threshold is lower and TPD (SRS) is expected to be dominant.

is intended to acknowledge the fact that while TPD has been observed to be a multibeam phenomenon, it may be the case that fewer beams contribute to SRS. The OMEGA experiment that produced the spectrum shown adjacent to Fig. 151.22(a) ($L_n \sim 150 \mu\text{m}$, $T_e \sim 2.5$ keV, $I \sim 6 \times 10^{14}$ W/cm²) is marginally unstable with respect to TPD and slightly less so to SRS if the total overlapped laser intensities are substituted into the expressions for the single-beam thresholds. In contrast, the NIF experiment at ignition-relevant conditions ($L_n \sim 525 \mu\text{m}$, $T_e \sim 4.5$ keV, $I \sim 1.3 \times 10^{15}$ W/cm²), which produced the spectrum shown in Fig. 151.22(a), is in the SRS-dominated regime: the threshold for SRS is exceeded by a factor of ~ 22 , while the TPD threshold is exceeded by a factor of ~ 6 . It is expected that this qualitative trend of SRS being increasingly prominent relative to TPD with increasing scale length and temperature³² applies also for more-complicated cases of multiple obliquely incident beams, although this is a subject of future work.

The broad spectral features seen in Figs. 151.22(a)–151.22(c) are characteristic of SRS occurring at densities below $n_c/4$ (between 0.15 and 0.22 n_c). Figures 151.22(b) and 151.22(c) highlight SRS spectra obtained at two different angles of observation and two distinct irradiation conditions. The target normal was parallel to the NIF polar axis [Fig. 151.22(f)], and the target was irradiated symmetrically, first by the outer beams from $t = 0$ to $t = 4.5$ ns, followed by the inner beams from $t = 4.5$ ns to $t = 7.5$ ns [Fig. 151.22(g)]. The predicted quarter-critical plasma conditions during the outer (inner) beam drive were $L_n \sim 500$ (690) μm , $I \sim 1.6$ (1.1) $\times 10^{15}$ W/cm², and $T_e \sim 4.7$ (4.4) keV, respectively. Temporally resolved scattered-light spectra²⁶ were obtained at 23.5° [Fig. 151.22(b)] and 50° [Fig. 151.22(c)]. SRS is observed by both diagnostics at early times during outer-beam irradiation and at later times when irradiated by the inner beams.

This observation is attributed to SRS sidescatter,³³ for which newly developed theory and supporting simulations are described in a companion manuscript.³⁴ In this process the SRS light waves propagate approximately tangentially to contours of constant electron density in the corona and see much greater gains relative to backscatter. The data shown in Figs. 151.22(b) and 151.22(c) are in agreement with the predictions of this theory and cannot be explained by narrow-angle backscatter simply caused by refraction, particularly for the SRS observed at 50°. Therefore, the propagation direction (and collection angle) of SRS light, after it has finished refracting and is in vacuum, is determined solely by its wavelength (i.e., the density where it was generated) and depends only weakly on the incidence angle of the beams that produced it. This is evident in Fig. 151.22(b), where SRS light at 23.5° is observed

at ~ 650 nm during both outer-beam and inner-beam irradiation. The SRS shifts to shorter wavelengths (~ 620 nm) when the observation angle is moved to 50° .

To determine the total amount of SRS generated in these experiments, absolutely calibrated photodiodes measured the SRS light collected in $\sim 2 \times 10^{-3}$ sr in the two full-aperture backscatter stations (FABS's)²⁶ at 50° and 30° . These measurements were then extrapolated to account for the total emission. This was accomplished using a ray-tracing code with plasma parameters and geometry provided by *DRACO* simulations to obtain simulated SRS emission profiles that include refraction and absorption as functions of wavelength and angle of observation (transmission of SRS light from its origin ranges from 2% at 702 nm to $\sim 50\%$ at 630 nm). These calculations assume 2π azimuthal symmetry around the target normal. With the above assumptions, it is estimated that between 2% and 6% of incident laser energy is converted to SRS light.

The inferred SRS light energy is compared to the energy in hot electrons, which is inferred from hard x-ray bremsstrahlung emission generated by the interaction of hot electrons with the target.³⁵ This bremsstrahlung emission was detected using the NIF filter fluorescer (FFLEX) diagnostic.³⁶ The FFLEX signals were analyzed by performing Monte Carlo electron-photon transport calculations with the *EGSnrc* code,³⁷ using a single-temperature (T_{hot}) 3-D Maxwellian hot-electron distribution. These calculations relate the absolute intensity of hard x-ray emission to the total quantity of hot electrons that produce it. Figure 151.24 shows the corresponding fraction of laser energy converted to hot electrons (f_{hot}) as a function of laser intensity at the quarter-critical density as calculated by *DRACO* for a series of experiments that include both CH and Si targets. The hard x-ray data were integrated over the period of the experiment starting after 4.5 ns. For outer-beam irradiation, f_{hot} increased from $0.7 \pm 0.2\%$ to $2.9 \pm 0.6\%$ as the laser intensity increased from 5.9×10^{14} W/cm² to 14×10^{14} W/cm². For inner-beam irradiation of CH targets, f_{hot} increased from $1.2 \pm 0.2\%$ to $2.6 \pm 0.5\%$ for intensities of 6.2×10^{14} W/cm² to 11×10^{14} W/cm². The uncertainty in f_{hot} is based on the statistical uncertainty in the single-temperature fit to the hard x-ray spectra. For CH experiments, T_{hot} is inferred to be between 45 and 55 keV for the outer-beam drive and 62 keV for the inner-beam drive, independent of laser intensity, with an uncertainty of ± 4 to 5 keV. The threshold intensity for the onset of measurable hot electrons in CH targets lies in the vicinity of 4×10^{14} W/cm².

The inferred energy and temperature of the hot electrons are consistent with simple arguments based on SRS being

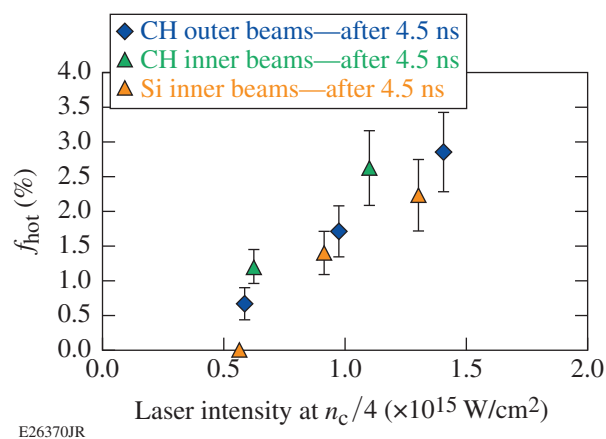


Figure 151.24

Fraction of laser energy converted to hot electrons as a function of quarter-critical laser intensity, for laser drive using outer beams (diamonds) and inner beams (triangles), for CH ablators (blue, green) and Si ablators (orange). The uncertainty in f_{hot} is based on the statistical uncertainty in T_{hot} extracted from the fit to the hard x-ray spectrum, propagated through *EGSnrc* modeling.

their source. By conserving wave action in the scattering process (i.e., the Manley–Rowe relations³⁸), it was determined that, for SRS wavelengths between 600 and 650 nm, the total energy in plasma waves is 70% to 85% of the total energy in SRS or between 1.4% and 5% of the incident laser energy for the experiments shown in Fig. 151.22. It is quite plausible that kinetic mechanisms such as wave breaking or stochastic processes can convert the plasma-wave energy into hot electrons with an efficiency sufficient to account for the fraction that is observed ($f_{\text{hot}} = 1\%$ to 3%). The characteristic temperature for SRS-generated electrons is often estimated by $T_\phi = (1/2) m_e v_\phi^2$ (Ref. 8), where v_ϕ is the phase velocity of the plasma wave. For our experiments, where SRS is observed from wavelengths of ~ 620 nm to ~ 702 nm ($2\lambda_0$), the corresponding hot-electron temperatures range from ~ 30 to ~ 85 keV ($T_\phi \sim m_e c^2/6$ for $n_e = n_c/4$), which is consistent with the hot-electron temperatures that best fit the measured hard x-ray spectrum.

The combination of T_{hot} and f_{hot} inferred in these experiments is close to the level that can be permitted in direct-drive-ignition designs, typically considered to be $f_{\text{hot}} \sim 0.5\%$ to 1% for $T_{\text{hot}} \sim 50$ keV (Refs. 2 and 39). This estimate is based on an allowable coupling of $\sim 0.1\%$ of laser energy to hot-electron preheat in the DT fuel and a near- 2π angular divergence of hot electrons inferred in OMEGA spherical experiments.²⁰ Based on these data, direct-drive-ignition designs using a CH ablator and quarter-critical laser intensities of $\sim 5 \times 10^{14}$ W/cm² may be acceptable, but for higher intensities, LPI mitigation is likely to be necessary. The discovery of a regime dominated by SRS, rather than by TPD as on OMEGA, necessitates a

re-evaluation of the angular divergence of hot electrons at direct-drive ignition-relevant conditions and may also require reconsideration of mitigation strategies.

One potential LPI mitigation strategy, originally proposed for TPD, uses strategically placed mid-Z layers in the ablator to locally shorten the density scale length, increase the electron temperature, enhance electron-ion collisional damping, and reduce Landau damping of ion-acoustic waves.^{40–45} This reduction in scale length and increase in temperature are predicted as well for planar Si experiments (L_n from $\sim 690 \mu\text{m}$ in CH to $\sim 560 \mu\text{m}$ in Si; T_e from $\sim 4.4 \text{ keV}$ in CH to $\sim 5.2 \text{ keV}$ in Si), for which hot-electron data are shown in Fig. 151.24. The use of Si ablaters has a modest effect on hot-electron levels, although it does increase the hot-electron intensity threshold to around $6 \times 10^{14} \text{ W/cm}^2$. The lack of hot electrons in this experiment also correlates with a minimal level of SRS observed in any of the spectrometers.

In summary, the first experiments to investigate LPI at direct-drive ignition-relevant coronal plasma conditions have revealed evidence of a regime dominated by SRS, with a significant contribution from tangential sidescatter. This result is in stark contrast to prior experiments on OMEGA at shorter scale lengths and lower temperatures, in which SRS was minimal and quarter-critical instabilities were identified as TPD. For the first time, intensity thresholds for LPI hot electrons have been evaluated at direct-drive-ignition scales, and the use of a Si ablator has been found to increase the threshold intensity slightly, from $\sim 4 \times 10^{14} \text{ W/cm}^2$ to $\sim 6 \times 10^{14} \text{ W/cm}^2$. These quarter-critical laser intensities present a viable design space for direct drive. As discussed, these results have implications for LPI hot-electron preheat mitigation in direct-drive-ignition designs, which traditionally have included strategies to mitigate TPD, but will have to consider SRS. In future experiments, it will be important to characterize the angular distribution of hot electrons, which strongly affects the tolerable level of hot-electron generation and may be different in this SRS-dominated regime than in TPD-dominated experiments on OMEGA.²⁰ Optical Thomson scattering will ultimately be used on the NIF^{46,47} to directly probe and characterize plasma waves in the quarter-critical region, as has been done previously on OMEGA,¹⁶ in order to definitively assess the presence or absence of TPD.

ACKNOWLEDGMENT

The authors thank NIF Operations and Target Fabrication Groups for their assistance in executing these experiments. This material is based upon work supported by the Department of Energy National Nuclear Security Administration under Award No. DE-NA0001944, the University of Roch-

ester, and the New York State Energy Research and Development Authority. The support of the DOE does not constitute an endorsement by the DOE of the views expressed in this article.

REFERENCES

1. J. Nuckolls *et al.*, *Nature* **239**, 139 (1972).
2. R. S. Craxton, K. S. Anderson, T. R. Boehly, V. N. Goncharov, D. R. Harding, J. P. Knauer, R. L. McCrory, P. W. McKenty, D. D. Meyerhofer, J. F. Myatt, A. J. Schmitt, J. D. Sethian, R. W. Short, S. Skupsky, W. Theobald, W. L. Kruer, K. Tanaka, R. Betti, T. J. B. Collins, J. A. Delettrez, S. X. Hu, J. A. Marozas, A. V. Maximov, D. T. Michel, P. B. Radha, S. P. Regan, T. C. Sangster, W. Seka, A. A. Solodov, J. M. Soures, C. Stoeckl, and J. D. Zuegel, *Phys. Plasmas* **22**, 110501 (2015).
3. G. H. Miller, E. I. Moses, and C. R. Wuest, *Opt. Eng.* **43**, 2841 (2004).
4. S. Atzeni and J. Meyer-ter-Vehn, *The Physics of Inertial Fusion: Beam Plasma Interaction, Hydrodynamics*, Hot Dense Matter, International Series of Monographs on Physics (Clarendon Press, Oxford, 2004).
5. D. W. Phillion *et al.*, *Phys. Fluids* **25**, 1434 (1982).
6. H. Figueroa *et al.*, *Phys. Fluids* **27**, 1887 (1984).
7. W. Seka, E. A. Williams, R. S. Craxton, L. M. Goldman, R. W. Short, and K. Tanaka, *Phys. Fluids* **27**, 2181 (1984).
8. W. L. Kruer, in *The Physics of Laser Plasma Interactions*, *Frontiers in Physics*, Vol. 73, edited by D. Pines (Addison-Wesley, Redwood City, CA, 1988). Chap. 4, pp. 37–43.
9. A. Simon, R. W. Short, E. A. Williams, and T. Dewandre, *Phys. Fluids* **26**, 3107 (1983).
10. C. S. Liu, M. N. Rosenbluth, and R. B. White, *Phys. Fluids* **17**, 1211 (1974).
11. N. A. Ebrahim *et al.*, *Phys. Rev. Lett.* **45**, 1179 (1980).
12. R. P. Drake, R. E. Turner, B. F. Lasinski, K. G. Estabrook, E. M. Campbell, C. L. Wang, D. W. Phillion, E. A. Williams, and W. L. Kruer, *Phys. Rev. Lett.* **53**, 1739 (1984).
13. C. Stoeckl, R. E. Bahr, B. Yaakobi, W. Seka, S. P. Regan, R. S. Craxton, J. A. Delettrez, R. W. Short, J. Myatt, A. V. Maximov, and H. Baldi, *Phys. Rev. Lett.* **90**, 235002 (2003).
14. D. T. Michel, A. V. Maximov, R. W. Short, S. X. Hu, J. F. Myatt, W. Seka, A. A. Solodov, B. Yaakobi, and D. H. Froula, *Phys. Rev. Lett.* **109**, 155007 (2012).
15. J. F. Myatt, J. Zhang, R. W. Short, A. V. Maximov, W. Seka, D. H. Froula, D. H. Edgell, D. T. Michel, I. V. Igumenshchev, D. E. Hinkel, P. Michel, and J. D. Moody, *Phys. Plasmas* **21**, 055501 (2014).
16. R. K. Follett, D. H. Edgell, R. J. Henchen, S. X. Hu, J. Katz, D. T. Michel, J. F. Myatt, J. Shaw, and D. H. Froula, *Phys. Rev. E* **91**, 031104(R) (2015).
17. P. Michel *et al.*, *Phys. Rev. Lett.* **115**, 055003 (2015).

18. S. Depierreux, C. Neuville, C. Baccou, V. Tassin, M. Casanova, P.-E. Masson-Laborde, N. Borisenko, A. Orekhov, A. Colaitis, A. Debayle, G. Duchateau, A. Heron, S. Huller, P. Loiseau, P. Nicolaï, D. Pesme, C. Riconda, G. Tran, R. Bahr, J. Katz, C. Stoeckl, W. Seka, V. Tikhonchuk, and C. Labaune, *Phys. Rev. Lett.* **117**, 235002 (2016).
19. W. Seka, J. F. Myatt, R. W. Short, D. H. Froula, J. Katz, V. N. Goncharov, and I. V. Igumenshchev, *Phys. Rev. Lett.* **112**, 145001 (2014).
20. B. Yaakobi, A. A. Solodov, J. F. Myatt, J. A. Delettrez, C. Stoeckl, and D. H. Froula, *Phys. Plasmas* **20**, 092706 (2013).
21. J. D. Lindl, *Phys. Plasmas* **2**, 3933 (1995).
22. T. R. Boehly, D. L. Brown, R. S. Craxton, R. L. Keck, J. P. Knauer, J. H. Kelly, T. J. Kessler, S. A. Kumpan, S. J. Loucks, S. A. Letzring, F. J. Marshall, R. L. McCrory, S. F. B. Morse, W. Seka, J. M. Soures, and C. P. Verdon, *Opt. Commun.* **133**, 495 (1997).
23. T. J. B. Collins, J. A. Marozas, K. S. Anderson, R. Betti, R. S. Craxton, J. A. Delettrez, V. N. Goncharov, D. R. Harding, F. J. Marshall, R. L. McCrory, D. D. Meyerhofer, P. W. McKenty, P. B. Radha, A. Shvydky, S. Skupsky, and J. D. Zuegel, *Phys. Plasmas* **19**, 056308 (2012).
24. S. Skupsky, R. W. Short, T. Kessler, R. S. Craxton, S. Letzring, and J. M. Soures, *J. Appl. Phys.* **66**, 3456 (1989).
25. I. V. Igumenshchev, D. H. Edgell, V. N. Goncharov, J. A. Delettrez, A. V. Maximov, J. F. Myatt, W. Seka, A. Shvydky, S. Skupsky, and C. Stoeckl, *Phys. Plasmas* **17**, 122708 (2010).
26. J. D. Moody *et al.*, *Rev. Sci. Instrum.* **81**, 10D921 (2010).
27. P. B. Radha, V. N. Goncharov, T. J. B. Collins, J. A. Delettrez, Y. Elbaz, V. Yu. Glebov, R. L. Keck, D. E. Keller, J. P. Knauer, J. A. Marozas, F. J. Marshall, P. W. McKenty, D. D. Meyerhofer, S. P. Regan, T. C. Sangster, D. Shvarts, S. Skupsky, Y. Srebro, R. P. J. Town, and C. Stoeckl, *Phys. Plasmas* **12**, 032702 (2005).
28. W. Seka, B. B. Afeyan, R. Boni, L. M. Goldman, R. W. Short, K. Tanaka, and T. W. Johnston, *Phys. Fluids* **28**, 2570 (1985).
29. T. Dewandre, J. R. Albritton, and E. A. Williams, *Phys. Fluids* **24**, 528 (1981).
30. The Doppler shift resulting from plasma flow affects the wavelength of both the incoming 351-nm light and the outgoing $\omega/2$ light, and constitutes an $\sim 10\%$ effect on the $\omega/2$ wavelength. The Dewandre shift results from plasma expansion and an increase in the plasma density between the quarter-critical region and the observer as $\omega/2$ propagates outward, and is an $\sim 2\%$ effect on the wavelength.
31. W. Seka, D. H. Edgell, J. F. Myatt, A. V. Maximov, R. W. Short, V. N. Goncharov, and H. A. Baldis, *Phys. Plasmas* **16**, 052701 (2009).
32. S. Weber and C. Riconda, *High Power Laser Sci. Eng.* **3**, e6 (2015).
33. B. B. Afeyan and E. A. Williams, *Phys. Fluids* **28**, 3397 (1985).
34. P. Michel, M. J. Rosenberg, T. Chapman, W. Seka, A. Solodov, R. W. Short, C. Goyon, M. Hohenberger, J. D. Moody, S. P. Regan, and J. F. Myatt, "Measurements and Modeling of Raman Side-Scatter in ICF Experiments," submitted to *Physical Review Letters*.
35. R. P. Drake, R. E. Turner, B. F. Lasinski, E. A. Williams, K. Estabrook, W. L. Kruer, E. M. Campbell, and T. W. Johnston, *Phys. Rev. A* **40**, 3219 (1989).
36. M. Hohenberger, F. Albert, N. E. Palmer, J. J. Lee, T. Döppner, L. Divol, E. L. Dewald, B. Bachmann, A. G. MacPhee, G. LaCaille, D. K. Bradley, and C. Stoeckl, *Rev. Sci. Instrum.* **85**, 11D501 (2014).
37. I. Kawrakow, *Med. Phys.* **27**, 485 (2000).
38. J. M. Manley and H. E. Rowe, *Proc. IRE* **44**, 904 (1956).
39. M. Hohenberger, P. B. Radha, J. F. Myatt, S. LePape, J. A. Marozas, F. J. Marshall, D. T. Michel, S. P. Regan, W. Seka, A. Shvydky, T. C. Sangster, J. W. Bates, R. Betti, T. R. Boehly, M. J. Bonino, D. T. Casey, T. J. B. Collins, R. S. Craxton, J. A. Delettrez, D. H. Edgell, R. Epstein, G. Fiksel, P. Fitzsimmons, J. A. Frenje, D. H. Froula, V. N. Goncharov, D. R. Harding, D. H. Kalantar, M. Karasik, T. J. Kessler, J. D. Kilkenny, J. P. Knauer, C. Kurz, M. Lafon, K. N. LaFortune, B. J. MacGowan, A. J. Mackinnon, A. G. MacPhee, R. L. McCrory, P. W. McKenty, J. F. Meeker, D. D. Meyerhofer, S. R. Nagel, A. Nikroo, S. Obenschain, R. D. Petrasso, J. E. Ralph, H. G. Rinderknecht, M. J. Rosenberg, A. J. Schmitt, R. J. Wallace, J. Weaver, C. Widmayer, S. Skupsky, A. A. Solodov, C. Stoeckl, B. Yaakobi, and J. D. Zuegel, *Phys. Plasmas* **22**, 056308 (2015).
40. R. E. Turner, K. Estabrook, R. L. Kauffman, D. R. Bach, R. P. Drake, D. W. Phillion, B. F. Lasinski, E. M. Campbell, W. L. Kruer, and E. A. Williams, *Phys. Rev. Lett.* **54**, 189 (1985); **54**, 1878(E) (1985).
41. V. A. Smalyuk, R. Betti, J. A. Delettrez, V. Yu. Glebov, D. D. Meyerhofer, P. B. Radha, S. P. Regan, T. C. Sangster, J. Sanz, W. Seka, C. Stoeckl, B. Yaakobi, J. A. Frenje, C. K. Li, R. D. Petrasso, and F. H. Séguin, *Phys. Rev. Lett.* **104**, 165002 (2010).
42. J. F. Myatt, H. X. Vu, D. F. DuBois, D. A. Russell, J. Zhang, R. W. Short, and A. V. Maximov, *Phys. Plasmas* **20**, 052705 (2013).
43. S. X. Hu, D. T. Michel, D. H. Edgell, D. H. Froula, R. K. Follett, V. N. Goncharov, J. F. Myatt, S. Skupsky, and B. Yaakobi, *Phys. Plasmas* **20**, 032704 (2013).
44. R. K. Follett, J. A. Delettrez, D. H. Edgell, V. N. Goncharov, R. J. Henchen, J. Katz, D. T. Michel, J. F. Myatt, J. Shaw, A. A. Solodov, C. Stoeckl, B. Yaakobi, and D. H. Froula, *Phys. Rev. Lett.* **116**, 155002 (2016).
45. J. R. Fein, J. P. Holloway, M. R. Trantham, P. A. Keiter, D. H. Edgell, D. H. Froula, D. Haberberger, Y. Frank, M. Fraenkel, E. Raicher, D. Shvarts, and R. P. Drake, *Phys. Plasmas* **24**, 032707 (2017).
46. P. Datte, J. S. Ross, D. Froula, J. Galbraith, S. Glenzer, B. Hatch, J. Kilkenny, O. Landen, A. M. Manuel, W. Molander, D. Montgomery, J. Moody, G. Swadling, J. Weaver, G. Vergel de Dios, and M. Vitalich, *J. Phys.: Conf. Ser.* **717**, 012089 (2016).
47. J. S. Ross, P. Datte, L. Divol, J. Galbraith, D. H. Froula, S. H. Glenzer, B. Hatch, J. Katz, J. Kilkenny, O. Landen, A. M. Manuel, W. Molander, D. S. Montgomery, J. D. Moody, G. Swadling, and J. Weaver, *Rev. Sci. Instrum.* **87**, 11E510 (2016).